JACS
JOURNAL OF THE AMERICAN CHEMICAL SOCIETY

ARTICLE

pubs.acs.org/JACS

Correlation between Atomic Coordination Structure and Enhanced Electrocatalytic Activity for Trimetallic Alloy Catalysts

Bridgid N. Wanjala,[†] Bin Fang,[†] Jin Luo,[†] Yongsheng Chen,[*,‡] Jun Yin,[†] Mark H. Engelhard,[§] Rameshwori Loukrakpam,[†] and Chuan-Jian Zhong[*,†]

[†]Department of Chemistry, State University of New York at Binghamton, Binghamton, New York 13902, United States

[‡]EMS Energy Institute, John and Willie Leone Family Department of Energy and Mineral Engineering, and Materials Research Institute, Pennsylvania State University, University Park, Pennsylvania 16802, United States

[§]EMSL, Pacific Northwest National Laboratory, Richland, Washington 99352, United States

Supporting Information

ABSTRACT: This Article describes findings of the correlation between the atomic scale structure and the electrocatalytic performance of nanoengineered PtNiFe/C catalysts treated at different temperatures for oxygen reduction reaction, aiming at providing a new fundamental insight into the role of the detailed atomic alloying and interaction structures of the catalysts in fuel cell reactions. Both mass and specific activities of the catalysts were determined using rotating disk electrode and proton exchange membrane fuel cell. The mass activities extracted from the kinetic regions in both measurements revealed a consistent trend of decreasing activity with increasing temperature. However, the specific activity data from RDE revealed an opposite trend, that is, increasing activity with increasing temperature. In addition to TEM, XRD, and XPS characterizations, a detailed XAFS analysis of the atomic scale coordination structures was carried out, revealing increased heteroatomic coordination with improved alloying structures for the catalyst treated at the elevated temperatures. XPS analysis has further revealed a reduced surface concentration of Pt for the catalyst for the high temperature treated catalyst. The higher mass activity for the lower temperature treated catalyst is due to Pt surface enrichment on the surface sites, whereas the higher specific activity for the higher temperature treated catalyst reflects an enhanced Pt-alloying surface sites. These findings have thus provided a new insight for assessing the structural correlation of the electrocatalytic activity with the fcc-type lattice change and the atomic scale alloying characteristics. Implications of these findings to the design of highly active alloy electrocatalysts are discussed, along with their enhanced electrocatalytic performance in the fuel cell.

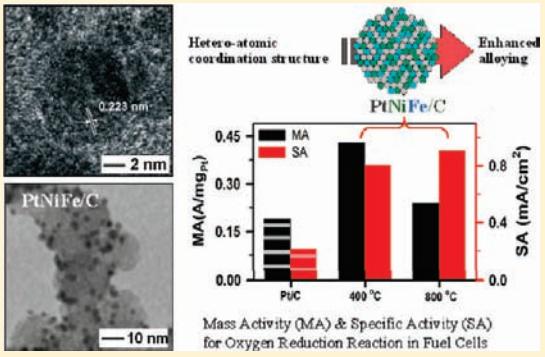

1. INTRODUCTION

Proton exchange membrane fuel cells (PEMFC) become increasingly attractive because of their high conversion efficiency, low pollution, light weight, high power density, and a wide range of applications from power sources in automobiles and space shuttles to power grids for buildings and factories. The high overall manufacturing cost of PEMFCs currently impedes, however, the commercialization of the fuel cell driven vehicles. The cost of the catalysts constitutes ~30% of the overall manufacturing cost because currently platinum is used as catalysts for both anodes and cathodes in PEMFCs.[1,2] Lowering of Pt-loading in the catalysts, improvement of the utilization of noble metals, and increase of the stability of catalysts are some of the current approaches to reducing the high cost of catalysts for the ultimate commercialization of PEMFCs. Pt alloys with early transition metals have attracted tremendous interest in the search for active catalysts for oxygen reduction reaction (ORR) in PEMFCs.[3−5] Because of structural changes caused by alloying Pt with other metals, some Pt-based alloys have been found to perform better in the ORR than pure Pt. For example, alloying Pt with some transition metals such as Co, Ni, Fe, Cr, Mn, V, etc., has been highlighted as a promising approach toward improved ORR. Studies on single crystalline thin films recently revealed that the addition of an early transition metal to Pt could change the atomic scale structures (Pt−Pt bond distance and coordination number) and electronic structures of Pt.[6,7] Because of these structural changes, the adsorption of OH is mostly on the second metal, and oxygen tends to be reduced on Pt in a "four electron" process. The ORR catalytic activity of these alloys is also dependent on the type and concentration of the second metal in the subsurface atomic layers.[8−11] These early studies on the model alloy catalysts indicate that an alloy nanoparticle (NP) of PtM where M = Fe, Co, or Ni, etc., exhibits an intermetallic structure. The development of Pt-based multimetallic or alloy

Received: May 2, 2011
Published: June 28, 2011

electrocatalysts is currently one promising area of finding effective solutions to the problem.[2]

Traditional catalyst-preparation methods such as coprecipitation and impregnation have been commonly used in the preparation of multimetallic or alloy catalysts, which are often not adequate for controlling the size and composition of the catalysts. We have developed a promising strategy for nanoengineering the size, shape, composition, and structural properties of multimetallic nanoparticles (e.g., AuPt, PtNi, PtCo, PtVFe, PtNiFe, PtNiCo, etc.) as active and stable electrocatalysts for ORR in fuel cell cathode reaction.[12−17] Examples of the catalysts that have demonstrated the viability for use in PEMFCs included nanoengineered AuPt, PtVFe, and PtNiFe catalysts.[17−20] For the trimetallic Pt-based catalysts prepared by our nanoengineered synthesis and processing,[21−24] the high electrocatalytic activity of the catalysts for ORR is a result of the introduction of a second or third metal with smaller atomic size than platinum, which produces a combination of reduction of the Pt−Pt distance, formation of metal−oxygen bond, and adsorption of hydroxide groups, and the modification of the d-band center. There have been limited reports on the detailed structural correlation with the fuel cell performance of Pt-based multimetallic alloy catalysts.[25−30] In this Article, we describe the results of a detailed structural characterization of the nanoengineered PtNiFe electrocatalysts, which have been shown to exhibit enhanced electrocatalytic performance in PEM fuel cells. In addition to correlating the nanostructures with the electrocatalytic activity, the fuel cell performance of the catalysts is also compared to other nanoengineered bimetallic and trimetallic catalysts in PEMFCs.

2. EXPERIMENTAL SECTION

Chemicals. Platinum(II) acetylacetonate ($Pt(acac)_2$, 97%) and nickel(II) acetylacetonate ($Ni(acac)_2$, anhydrous, >95%) were purchased from Strem Chemicals. Iron(II) acetylacetonate ($Fe(acac)_2$, 99.95%), 1,2-hexadecanediol ($CH_3-(CH_2)_{13}-CH(-OH)-CH_2-OH$, 90%), octyl ether ($[CH_3(CH_2)_7]_2O$, 99%), oleylamine ($CH_3(CH_2)_7CH{=}CH(CH_2)_8NH_2$, 70%), oleic acid ($CH_3(CH_2)_7CH{=}CH(CH_2)_7COOH$, 99+%), and Nafion solution (5 wt %) were purchased from Aldrich. Optima grade perchloric acid was purchased from Fisher Scientific. Other solvents such as ethanol and hexane were purchased from Fisher. All chemicals were used as received.

Catalyst Preparation. The synthesis of PtNiFe nanoparticles followed the synthesis protocol reported previously.[24] Briefly, the synthesis involved mixing three metal precursors, $Pt^{II}(acac)_2$, $Ni^{II}(acac)_2$, and $Fe^{II}(acac)_2$, in controlled molar ratios, which underwent reduction by 1,2-hexadecanediol in an octyl ether solvent in the presence of a mixture of oleylamine and oleic acid as capping agents.

The as-synthesized PtNiFe nanoparticles were supported on carbon black and subsequently thermally treated. Details of the synthesis, preparation, and thermal treatment are described in previous reports.[24] Briefly, 810 mg of carbon black (ECP, Ketjen Black International, Tokyo) and 202.5 mg of the as-synthesized PtNiFe nanoparticles were used to produce the carbon-supported PtNiFe catalysts (PtNiFe/C). The thermal treatment involved first treatment at 280 °C under 20% O_2 followed by treatment at 400−800 °C under 15% H_2. The actual loading was determined by TGA method.

Electrochemical Measurements. Glassy carbon (GC) disks (geometric area: 0.196 cm^2) were polished with 0.05 μm Al_2O_3 powders, followed by careful rinsing with deionized water. The geometric area of the GC electrode provides a measure of the loading of catalyst on the electrode surface used for the voltammetric characterization. The electrode was coated with the catalyst layer using a modified method from a previous report.[21,24] Briefly, a typical suspension of the catalyst was prepared by suspending 1.0 mg of catalyst (PtNiFe/C) in 1 mL of Millipore water with diluted (5% vol.) Nafion (5 wt %, Aldrich). The catalyst suspension (ink) was then quantitatively transferred to the surface of the polished GC disk. The electrodes were dried overnight at room temperature.

Membrane Electrode Assemblies (MEAs). The MEAs (5 cm^2 active area) used in this study were prepared by conventional catalyst coated substrate (CCS) method. The electrocatalyst-Nafion ink was painted on a wet-proofed carbon paper (Toray EC-TP1-060T). The MEAs were prepared using $Pt_{46}Ni_{22}Fe_{32}$/C catalyst (metal loading: 27% for 400 °C sample and 37% for 800 °C, 0.4 mg_{Pt}/cm^2) for the cathode and Pt/C catalyst (20% Pt/C, E-tek, 0.4 mg_{Pt}/cm^2) for the anode. For comparison, MEAs were also prepared using Pt/C (20% Pt/C, E-tek, 0.4 mg $_{Pt}/cm^2$) catalyst for both anode and cathode. The MEAs were prepared by hot pressing the sandwich structured Nafion 212 membrane (DuPont) and catalyst coated electrodes at 120 °C. The MEAs were tested in a single-cell test station (Electrochem Inc.). The testing conditions included 100% humidified H_2 and O_2 at a flow rate of 100 mL/min, a back pressure of 30 psi for both electrodes, and an operating temperature of 75 °C.

Instrumental Characterizations. Inductively coupled plasma − optical emission spectroscopy (ICP-OES) was used to analyze the composition, which was performed using a Perkin-Elmer 2000 DV ICP-OES utilizing a cross-flow nebulizer with the following parameters: plasma 18.0 L $Ar_{(g)}$/min; auxiliary 0.3 L $Ar_{(g)}$/min; nebulizer 0.73 L $Ar_{(g)}$/min; power 1500 W; peristaltic pump rate 1.40 mL/min. Elements <1.0 mg/L were analyzed using a Meinhardt nebulizer coupled to a cyclonic spray chamber to increase analyte sensitivity with the following parameters: 18.0 L $Ar_{(g)}$/min; auxiliary 0.3 L $Ar_{(g)}$/min; nebulizer 0.63 L $Ar_{(g)}$/min; power 1500 W; peristaltic pump rate 1.00 mL/min. Elemental concentrations were determined by measuring one or more emission lines (nm) to check for interferences: Pt 203.646, Ni 221.647, and Fe 238.204. The nanoparticle samples were dissolved in concentrated aqua regia and then diluted to concentrations in the range of 1−50 ppm for analysis. Multipoint calibration curves were made from dissolved standards with concentrations from 0 to 50 ppm in the same acid matrix as the unknowns. Laboratory check standards were analyzed every 6 or 12 samples, with instrument recalibration if check standards were not within ±5% of the initial concentration. Method detection limits were determined using 1.0 mg/L of analyte in the same acid matrix and are reported in mg/L as follows: Pt < 0.040 and Ni < 0.026, Fe < 0.016. Instrument reproducibility (n = 10) determined using 1 mg/L elemental solutions resulted in <±2% error for all three elements.

Direct Current Plasma-Atomic Emission Spectroscopy (DCP-AES) technique was used to analyze the composition, which was performed using an ARL Fisons SS-7 direct current plasma-atomic emission spectrometer. Measurements were made on emission peaks at 265.95, 231.60, and 259.94 nm for Pt, Ni, and Fe, respectively. The nanoparticle samples were dissolved in concentrated aqua regia and then diluted to concentrations in the range of 1−50 ppm for analysis. Calibration curves were made from dissolved standards with concentrations from 0 to 50 ppm in the same acid matrix as the unknowns. Instrument reproducibility, for concentrations greater than 100 times the detection limit, results in <±2% error.

Transmission electron microscopy (TEM) was performed on a Hitachi H-7000 electron microscope (100 kV) to obtain the particle size and its distribution. HRTEM was carried out using a JEOL JEM 2010F at an acceleration voltage of 200 kV. The microcompositions of individual nanoparticles of the powder catalysts were analyzed on a Hitachi HD-2000 transmission electron microscope equipped with EDS in TEM mode. For TEM measurements, nanoparticles samples were diluted in hexane solution and were drop cast onto a carbon-coated copper grid followed by solvent evaporation in air at room temperature.

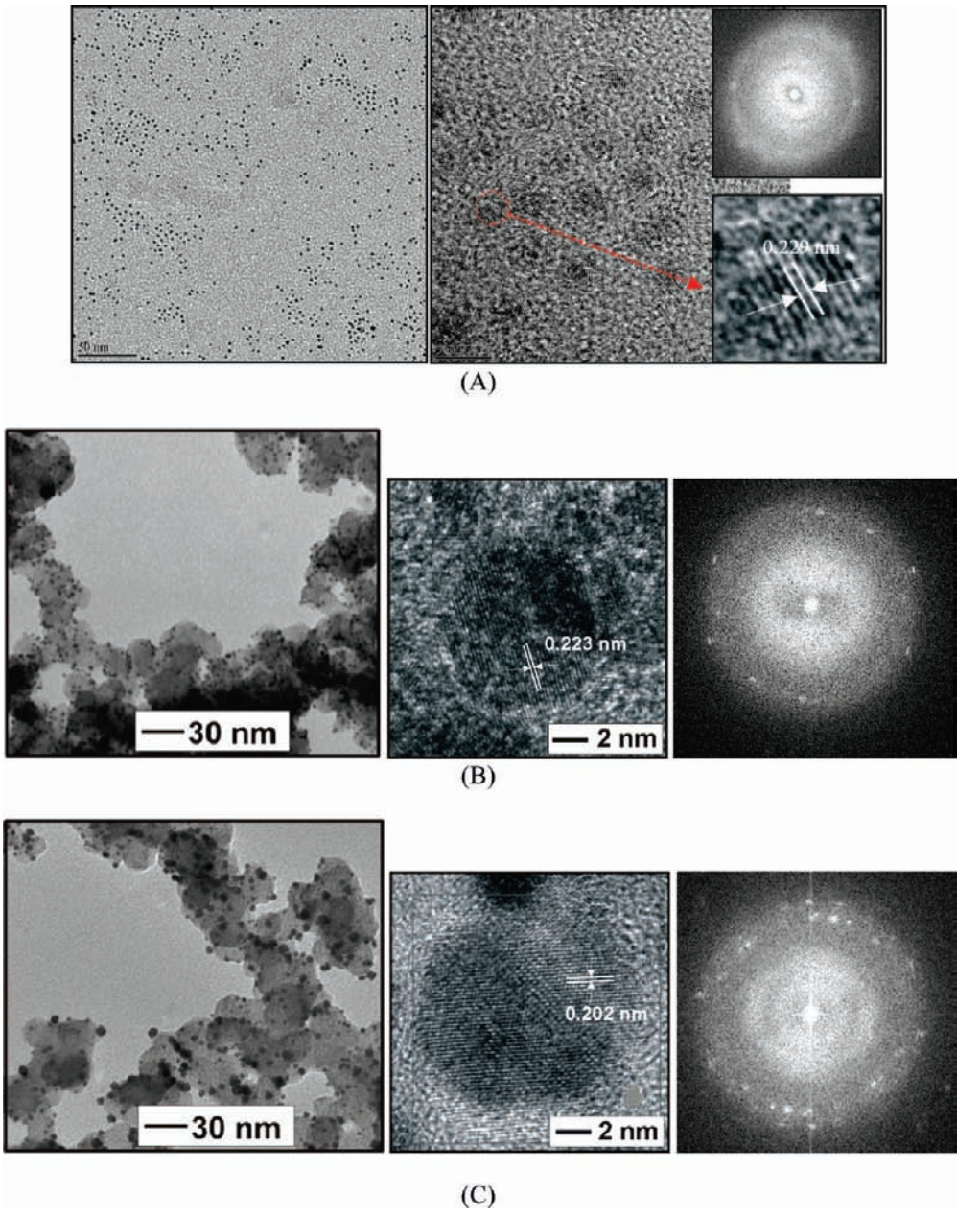

Figure 1. TEM micrographs and HRTEM/FFTs for the as-synthesized $Pt_{46}Ni_{22}Fe_{32}$ nanoparticles (A, 3.0 ± 0.3 nm), and $Pt_{46}Ni_{22}Fe_{32}$/C catalysts annealed at 400 °C (B, 5.3 ± 0.4 nm) and 800 °C (C, 7.8 ± 0.6 nm).

Thermogravimetric analysis (TGA) was performed on a Perkin-Elmer Pyris 1-TGA for determining the weight of organic shell and metal loading on carbon. Typical samples weighed ~4 mg and were heated in a platinum pan. Samples were heated in 20% O_2 at a rate of 10 °C/min.

X-ray powder diffraction (XRD) was used to measure the lattice constants and to estimate particle sizes of the catalysts. XRD data were collected from 20° to 90° for 2θ with a step size of 0.5° at room temperature on a Phillips X'pert PW 3040 MPD diffractometer using Cu Kα line (λ = 1.5418 Å), equipped with a sealed Xe proportional detector and a diffracted beam graphite monochromator, which filter out all but Kα radiation. The diffraction data were compared to the XRD database of the International Centre for Diffraction Data (ICDD) for phase identification.

X-ray photoelectron spectroscopy (XPS) measurements were performed to identify the oxidation states and atomic percentages of Pt, Ni, and Fe on the surface of the catalysts. The XPS measurements were made by using a Physical Electronics 5000 versa probe scanning ESCA microprobe. This system used a focused monochromatic Al Kα (1486.7 eV) X-ray source for excitation and a spherical section analyzer. The instrument had a 16-element multichannel detection system. The X-ray beam used was a 100 W, 200 μm-diameter beam. The X-ray beam was incident normal to the sample, and the X-ray detector was at 45° off-normal using an analyzer angular acceptance width of 20° × 20°. Wide scan data were collected using a pass energy of 187.85 eV. The binding energy (BE) scale was calibrated using Cu $2p_{3/2}$ feature at 932.58 ± 0.05 eV and Au $4f_{7/2}$ at 84.01 ± 0.05 eV for known standards. The samples experienced variable degrees of charging, and low energy electrons at ~1.5 eV, 20 μA, and low energy Ar^+ ions were used to minimize the charging. The percentages of individual elements detected were determined from the relative composition analysis of the peak areas of the bands.

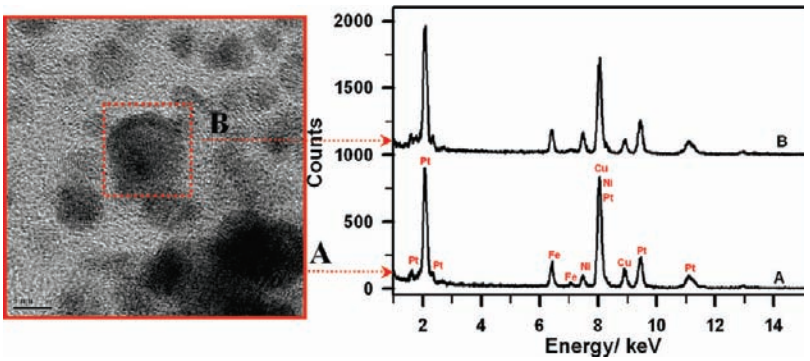

Figure 2. HRTEM-EDX analysis for a selected area of nanoparticles (A) and one individual particle (B) identified in the HRTEM image (left) for a $Pt_{46}Ni_{22}Fe_{32}/C$ catalyst sample treated at 800 °C. Compositions from the EDS data analysis (PtLa and Lb, Ni Ka, Fe Ka): (A) $Pt_{39}Ni_{23}Fe_{38}$ and (B) $Pt_{36}Ni_{29}Fe_{35}$.

X-ray absorption fine structure spectroscopy (XAFS) was performed as follows. Pt L3 edge (11 564 eV) and Ni K edge (8333 eV) XAFS spectra were collected on the insertion device beamline of the Materials Research Collaborative Access Team (MRCAT) at the Advanced Photon Source (APS), Argonne National Laboratory. Fe K edge (7112 eV) XAFS spectra were collected on the bending magnet beamline 9-BM-B at APS. A double-crystal Si (111) monochromator was used along with a Rh-coated mirror to reduce harmonics. All spectra were collected in transmission mode. Powder samples were pressed into pellets with optimal thickness to ensure good quality data. X-ray intensity of the sample was measured by ionization chambers filled with N_2. In addition, a reference spectrum of Pt, Ni, or Fe foil for energy calibration was collected simultaneously with each scan using an additional ionization chamber.

Practically, XAFS can be divided into two regions, near-edge region and extended region. The near-edge XAFS, or X-ray absorption near edge structure (XANES) spectroscopy, provides information on oxidation state, coordination symmetry, and can be used for identification of different species by fingerprinting. In contrast, extended XAFS, or EXAFS, measures the coordination structure including bond distance and coordination number of neighboring atoms. A detailed description of XANES and EXAFS theory and data processing was provided elsewhere.[31] XANES spectra were processed using Athena.[32] EXAFS oscillations were extracted using Athena, and fitting of EXAFS data was performed using Artemis[32] and scattering paths generated by the FEFF code (version 6.0).[33] The fitting was limited to 2.0−16.0 $Å^{-1}$ for Pt L3 edge spectra and 2.0−13.0 $Å^{-1}$ for Ni and Fe K edge spectra, using a Hanning window with $dk = 1.0$ $Å^{-1}$. The fits were performed to both the real and the imaginary parts of $\chi(R)$ in the region of 1.0 Å < R < 3.2 Å. Similar analysis was performed on reference samples Pt, Ni, and Fe foils to obtain S_0^2, the amplitude reduction factor, for the subsequent determination of the coordination numbers of the fitted structure of the samples. The structure at distances greater than 3.5 Å contains information about outer coordination shells and can be useful for determining particle size for simple systems such as monodispersed pure metal particles. We did not attempt to fit these features because the trimetallic nanoparticle system studied here is rather complicated due to the presence of three different phases: oxide, alloy, and metal phase, all of which contribute to the EXAFS structure above 3.5 Å. This makes it difficult if not impossible to build a reasonable molecular model structure to fit the structure.

We also note that Fe and Ni have very similar scattering features because of their almost identical atomic numbers (Fe(26) and Ni (28)) and atomic radii (the difference is about 0.005 Å). Consequently, it is impossible to resolve their coordination structure independently by performing individual or global fitting of EXAFS data. In this work, we developed a method to evaluate the coordination structure involving very similar elements such as Fe and Ni. For example, when fitting the Pt EXAFS data, we used two different models (i.e.,"PtNi" and "PtFe" models), in which either Fe or Ni was used to represent both Fe and Ni. Each model was not perfect but reasonable, and the fitting results were closely examined.

3. RESULTS AND DISCUSSION

3.1. Morphology, Composition, and Crystallinity. *Nanoparticle Morphology.* The as-synthesized PtNiFe nanoparticles were easily dispersed in nonpolar solvents such as hexane, which is consistent with the presence of a monolayer of surfactants on the surface of the particles.[24] Figure 1A shows a representative TEM micrograph for a sample of the as-synthesized PtNiFe nanoparticles. The nanoparticles are highly monodispersed. The particle sizes are very well controlled with an average size of 3.0 ± 0.4 nm (Supporting Information, Figure S1). The fact that the individual nanoparticles are well separated is indicative of the encapsulation of the nanocrystal cores by the organic monolayers (oleylamine and oleic acid), which was previously confirmed by FTIR.[24]

Figure 1B,C shows a representative set of TEM micrographs for the PtNiFe catalyst after thermal treatments at different temperatures. The average sizes of the carbon-supported catalysts after the thermal treatment were found to depend on the thermal treatment temperature. The catalysts described in this Article showed an average size of 5.3 ± 0.4 nm for the treatment temperature of 400 °C and 7.8 ± 0.6 nm for the treatment temperature of 800 °C (Supporting Information, Figure S1).

Bulk and Nanoparticle Compositions. Bulk compositions of the as-synthesized and the supported PtNiFe nanoparticles, which were determined by ICP-OES or DCP-AES methods, were found to depend only on the synthesis condition, the details of which were reported previously.[24] One important question on the multimetallic nanoparticles is whether the nanoparticles are multimetallic in individual nanoparticles or in an ensemble of the nanoparticles. To answer the question, high resolution TEM coupled with energy dispersive X-ray spectroscopy (HRTEM-EDS) was employed. The HRTEM-EDS data are also compared to DCP-AES analysis (macro-composition).[24] By carefully controlling the electron beam diameter and current, this measurement can yield reproducible compositions of individually isolated

nanoparticles. Figure 2 shows a set of HRTEM-EDS data for a sample of $Pt_{46}Ni_{22}Fe_{32}$/C catalyst treated at 800 °C in a selected area of nanoparticles (A) and one individual nanoparticle (B). An analysis of these EDS data revealed the composition of $Pt_{39}Ni_{23}Fe_{38}$ for (A) and $Pt_{36}Ni_{29}Fe_{35}$ for (B). These atomic percentages for Ni and Fe are very close to the bulk analysis data ($Pt_{46}Ni_{22}Fe_{32}$). The somewhat smaller atomic percentage for Pt is believed to be due to the presence of a small fraction of small particles, which were not sampled in the analysis area. This assessment was supported by another set of data for a sample of PtNiFe/C catalysts with a different composition (Supporting Information, Figure S2), which was found to show some degree of variation with the particle size. Similar compositions were found for C-supported PtNiFe nanoparticles before the thermal treatment, indicating that the subtle composition variation likely originated from the presence of Ni in the nanoparticles and nanoparticle sintering.[14] This situation was unlike the uniform compositions observed for PtVFe nanoparticles in our previous work,[23] which is in contrast to those catalysts prepared by traditional synthesis methods where large particles are usually base metal rich and small particles are Pt rich.

Nanoparticle Crystallinity. The crystal structure and crystallite size in the catalysts were characterized using X-ray diffraction. Figure 3 shows XRD patterns for PtNiFe/C catalysts after the thermal treatment at two different temperatures: 400 °C (a) and 800 °C (b). Generally, the observed diffraction patterns are consistent with fcc structure, and the diffraction peaks are identified and indexed, such as (111), (200), (220), (311), and (222) reflections. The average crystallite size of the catalysts was also estimated utilizing Scherrer's equation relating the coherently scattering domains with Bragg peak widths:

$$L = \frac{k\lambda}{\beta \cos(\theta)}$$

where $k = 0.89$ for spherical particles, λ is the wavelength of the radiation used (λ = 0.15418 nm), β is the full width at half-maximum of the peak in radians, and θ is the Bragg angle. We estimated the average size of the PtNiFe/C catalysts annealed at 400 and 800 °C from the (111) peak positions of the corresponding X-ray diffraction patterns. While it is known that the crystallite size equals particle size if the particles are single crystals, the estimated sizes of 4.9 and 7.4 nm for the 400 and 800 °C PtNiFe particles are very similar to the TEM-determined results, demonstrating a high degree of crystallinity for the nanoparticle catalysts. The subtle difference could reflect the fact that there was some degree of nonuniformity of particle sizes in the nanoparticles.

A close examination of the peak position reveals some additional peaks in addition to the regular fcc diffraction pattern. In comparison with the database for single metallic component, there is no evidence of phase segregation, indicating that the PtNiFe catalysts are single-phase alloy at low and high treatment temperatures. It is also observed that there are extra diffraction peaks other than the fcc-type diffraction peaks (41.1° (111), 47.9° (200), 70.0° (220), 83.9° (311) for the 400 °C treated catalyst; and 41.4° (111), 48.0° (200), 71.0° (220), 84.6° (311) for the 800 °C treated catalyst), which could be due to the formation of a structure that is fct in nature or the presence of impurities in the catalysts whose percentage increases at higher treatment temperature (e.g., small peaks such as 33.1°, 49.7°,

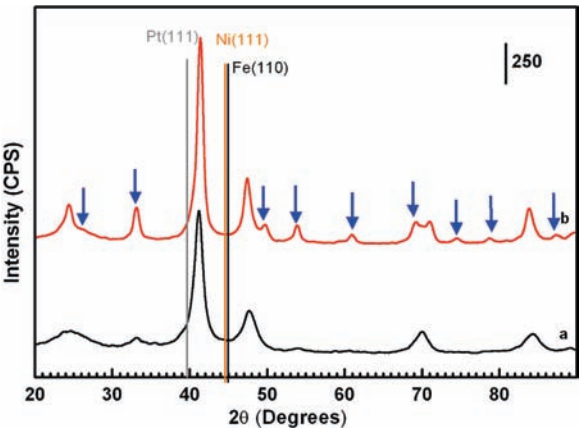

Figure 3. XRD patterns for $Pt_{46}Ni_{22}Fe_{32}$ catalysts treated at different temperatures: 400 °C (a) and 800 °C (b). Blue arrows indicate additional peaks to regular fcc diffraction peaks.

53.9°, 61.0°, 71.2°, 74.5°, 78.9°, and 87.5° for the 800 °C treated PtNiFe catalyst). A shift in (111)-peak position (and for the other peaks as well) toward higher angles with an increase of annealing temperature was observed. This is attributed to a very small lattice shrinking as the thermal treatment temperature is increased. The lattice constant for the catalyst annealed at low temperature was estimated to be 0.3798 nm, which is slightly larger than that for the catalyst annealed at higher treatment temperature (0.3780 nm). A similar trend in peak shifting was also observed for the other peaks. The replacement of a Pt atom by Ni/Fe atoms is believed to lead to the observed reduction of the lattice constant, resulting in a better alloy structure for the higher temperature treated catalyst.

We also studied other compositions, for example, $Pt_{28}Ni_{18}Fe_{53}$/C, as a function of treatment temperature (Figure S3). The XRD patterns were quite consistent with those shown in Figure 3. In addition to the structural assessment above, it is also possible that a tetragonal-type structure of the PtFe type is formed upon annealing. It is not exactly clear how Ni, Fe, and Pt are arranged on the tetragonal lattice sites. One possibility could be that the structure is initially quite disordered but transforms to the tetragonal FePt type due to the presence of Ni in this case. Fe and Ni may substitute each other, so we may have a ternary alloy of the tetragonal type (Fe/Ni)Pt. No signature of a second phase (e.g., phase-segregated Pt, Ni, or Fe) was observed in this case. The particles size was observed to increase with treatment temperature in this composition, and the system underwent a phase transition, from a disordered state to a tetragonal Fe/Ni Pt phase type. However, this possibility is yet to be examined because the nanostructure is quite disordered.

Surface Composition. The XPS characterization was employed to provide insights into the surface composition of the PtNiFe/C electrocatalysts treated at two different temperatures. Figure 4A−C shows XPS spectra in the Pt 4f, Ni 2p, and Fe 2p regions in the PtNiFe/C samples annealed at 400 and 800 °C. Pt $4f_{7/2}$ and Pt $4f_{5/2}$ bands were observed at 71.9 and 75.2 eV for 400 °C, and 71.9 and 75.2 eV at 800 °C, respectively. The Pt 4f values for these catalysts were found to be in agreement with the literature values (70.5−72.0 eV) for the binary and ternary alloy systems prepared by similar/other techniques.[16,35−37] Our previous study of PtNiCo catalyst reported different Pt oxides

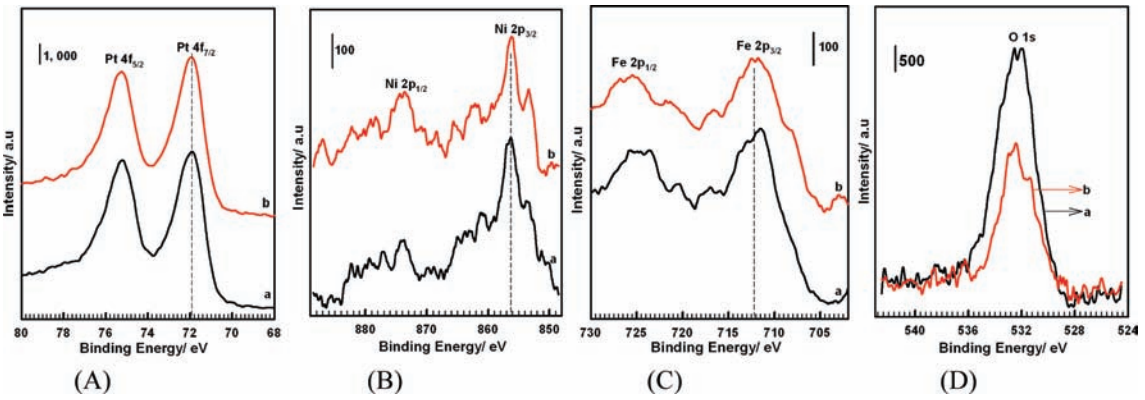

Figure 4. XPS spectra in the Pt4f (A), Ni 2p (B), Fe2p (C), and O1s (D) regions for $Pt_{46}Ni_{22}Fe_{32}/C$ catalysts treated at 400 °C (a) and 800 °C (b) (the scale numbers are in arbitrary units).

Table 1. Comparison of Binding Energy (BE) Values (in eV) and Relative Composition (in atomic %) for $Pt_{46}Ni_{22}Fe_{32}/C$ Catalysts Treated at the Two Different Temperatures[a]

	binding energy (eV) and Pt:Ni:Fe composition (%)			
	400 °C		800 °C	
bands	eV	Pt:Ni:Fe (%)	eV	Pt:Ni:Fe (%)
Pt $4f_{7/2}$	71.9	$Pt_{46}Ni_{19}Fe_{35}$	71.9	$Pt_{43}Ni_{23}Fe_{34}$
Pt $4f_{5/2}$	75.2		75.2	
Ni $2p_{3/2}$	856.2		856.2	
Ni $2p_{1/2}$	873.6		873.2	
Fe $2p_{3/2}$	712.0		712.0	
Fe $2p_{1/2}$	725.5		725.5	

[a] Standard deviation: ±0.05 eV for binding energy value and ±5% for the composition ratio.

including Pt^{2+} (72.7−73.0 eV) and Pt^{4+} (73.9−75.8 eV) that were in agreement with literature values.[35−37] The Ni $2p_{3/2}$ and Ni $2p_{1/2}$ peaks were observed at 856.2 and 873.6 eV for 400 °C, and 856.2 and 873.6 eV for 800 °C, also suggesting the presence of higher oxidation state oxide components and metal oxides in our catalysts treated at both temperatures. These results were also found to be in agreement with our previous findings from a related PtNiCo system[16] and with other literature values.[35−37] For example, Shukla and co-workers reported Ni$2p_{3/2}$ values at 855.0 eV for Ni^0, 856.1 eV for Ni^{2+} ($Ni(OH)_2$), for bimetallic PtNi nanoparticles.[36] In addition to the alloying/support effect, the shift to higher oxidation states in our PtNiFe/C catalysts is attributed to the presence of higher oxidation state components in the form of metal oxides. The Fe $2p_{3/2}$ and Fe $2p_{1/2}$ peaks were observed at 712.0 and 724.6 eV for 400 °C, and 712.0 and 725.5 eV for 800 °C, respectively, slightly shifted to higher energy (707.0−710.3 eV)[38−40] by approximately 2 eV due to the presence of higher oxidation state components (e.g., FeO_x). Literature values show the presence of different oxidation states of Fe_xO_y at the following (FeO (710.3 eV); Fe_2O_3 (711.3 eV); Fe_3O_4 (711.4 eV)) energy levels.[41,42]

Table 1 summarizes BE values (in eV) and the relative composition values for PtNiFe catalysts treated at the two different temperatures. The BE values for Pt $4f_{7/2}$ and $4f_{5/2}$, Ni $2p_{3/2}$ and $2p_{1/2}$, and Fe $2p_{3/2}$ and $2p_{1/2}$ are practically identical for the two temperatures. The relative surface compositions determined from the XPS data yielded "$Pt_{46}Ni_{19}Fe_{35}/C$ and $Pt_{43}Ni_{23}Fe_{34}$" as the metal ratios for 400 and 800 °C treatments, respectively. A comparison between the low and high treated catalysts revealed some base metal enrichment effect in the higher temperature treated catalyst where some small percentage of Pt in the surface is replaced by the base metals, indicating a certain degree of enrichment of Ni and Fe on the alloy surface for the catalyst treated at this condition.

In addition to the metal ratios and the carbon support, oxygen species were detected for the PtNiFe catalysts annealed at 400 and 800 °C. In the O 1s region (Figure 4D), the O 1s peaks are observed at ∼532.2 eV for both 400 and 800 °C treated catalysts, signifying the presence of oxide species. On the basis of the analysis of the intensity of the O 1s peaks, the oxide species detected for the catalyst treated at higher temperature was found to be much lower (2.6% O) than that of the catalyst treated at lower treatment temperature (5.2% O%). Clearly, there is a decrease in oxygenated species from 400 to 800 °C, reflecting the likelihood of the surface area decrease from the smaller-sized particles treated at 400 °C (5.3 nm) to the larger-sized particles treated at 800 °C (7.8 nm), which corresponds to about 50% decrease in total surface area.

3.2. Atomic Coordination and Interaction in Alloys. To gain further insight into the electronic/coordination structures of the PtNiFe catalysts, XAFS measurements were carried out, focusing on the $Pt_{46}Ni_{22}Fe_{32}/C$ catalysts treated at 400 and 800 °C. Figure 5 shows normalized Pt L3 and Ni K edge XANES spectra for the catalysts. For comparison, XANES spectra for Ni and Pt foils are also shown. Both catalysts show slightly higher white line (at around 11 567 eV) intensities than that of Pt foil. These small changes could be due to a decrease of 5d orbital filling in the Pt alloys as a result of oxidation and hybridization (increased Pt d-band vacancies). The intensity of the Ni K pre-edge peak (at around 8335 eV) for PtNiFe/C catalysts decreases, while the white line (at around 8350 eV) intensity increases as compared to the Ni foil (Figure 5B). These changes demonstrated the strong hybridization between Pt and Ni and/or the formation of Ni oxides.[9,16]

More quantitative structural information on the PtNiFe/C catalyst after different heat treatments is obtained through fitting of the EXAFS data. We collected EXAFS spectra at Pt L3 and Ni K-edge (Fe K-edge EXAFS was also collected for the low temperature sample). The Pt EXAFS is of very high quality, and

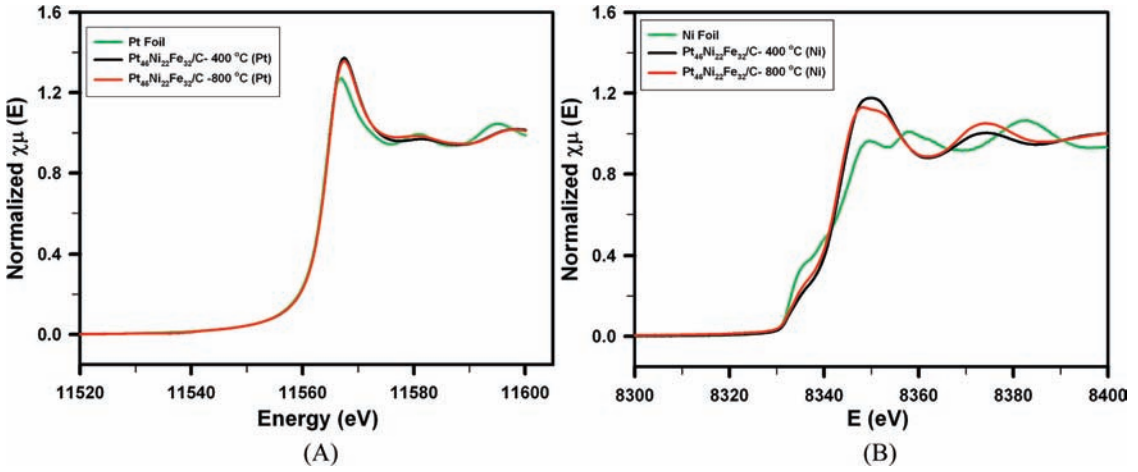

Figure 5. Normalized XANES spectra at Pt L3 edge and Ni K edge for $Pt_{46}Ni_{22}Fe_{32}$ catalyst treated at 400 and 800 °C. Note that the green curves in (A) and (B) are for Pt and Ni references, respectively.

the Ni EXAFS is reasonably good (see chi(k) data in the Supporting Information). One may hope that Pt EXAFS provides quantitative information about Pt alloying with Fe and Ni. The difficulty lies in the fact that Fe and Ni have very similar scattering features because of their almost identical atomic number (Fe(26) and Ni (28)) and atomic radius (the difference is about 0.005 Å). Consequently, it is almost impossible to distinguish them when both are present in the first coordination shell only by fitting of Pt EXAFS data. In this work, we developed a method to evaluate the coordination structure involving very similar elements. Both individual (Supporting Information, Figure S4) and global fittings of the EXAFS data were performed using different model structures of the PtNiFe nanoparticles, and the results are discussed in the following two subsections.

Pt Coordination Structure. It was found that Pt EXAFS could be well fitted with O, Pt, Ni (PtNi model) or O, Pt, Fe (PtFe model) in the first coordination shell. However, including both Ni and Fe would not result in good fit without placing constraints on Fe and Ni. Therefore, fitting was performed by including either Ni or Fe in the model structure. Both models resulted in similarly good fit of the EXAFS data (Supporting Information, Figure S4) for the catalysts treated at 400 and 800 °C, and the fitted parameters are presented in Table S1. Comparing the results for the same PtNiFe/C catalyst treated at 400 and 800 °C from the two models, we found that the fitted parameters for Pt neighbors including coordination number (CN), bond distance , and Debye−Waller factor (or bond disorder) are basically the same (or not significantly different) within the uncertainties associated with the parameters from the two models used. The fitted bond distance for Pt−Ni or Pt−Fe is almost the same. There is a slight difference in the fitted coordination number and bond disorder for Pt−Ni and Pt−Fe. The observations suggest the following: (1) structural information for Pt−Pt can be reliably retrieved from the Pt L3 edge EXAFS data; (2) in the PtNiFe/C catalysts treated at 400 and 800 °C, both Fe and Ni are nearest neighbors around Pt, thus directly proving the existence of Pt alloy; and (3) the fitted coordination numbers of Ni and Fe (from two separate fits using different models) provide a range of coordination number of combined Ni and Fe neighbors.

There are other important observations when comparing the fitting results of PtNiFe/C catalysts treated at 400 and 800 °C using the same model (either PtNi or PtFe model). The fitted bond distance and bond disorder for a specific neighbor (e.g., Pt or Ni) in both catalysts are basically the same (or not significantly different) within the associated uncertainties. The main difference between PtNiFe/C catalysts treated at 400 and 800 °C is the coordination number. This lays the ground for performing a global fitting to both catalysts with the assumptions that a specific neighbor shares the same bond distance and same bond disorder in the two catalysts, which is shown to be an effective way to reduce uncertainties associated with fitted parameters.

Fitted parameters from the global fitting of the Pt L3 edge EXAFS spectra for PtNiFe/C catalysts treated at 400 and 800 °C are presented in Table 2. The original and fitted magnitudes of Fourier transformed k^2-weighted Pt L3 edge EXAFS spectra are shown in Figure 6. A comparison of the results from global fitting (Table 2) and individual fittings (Table S1) of two similar systems shows that the global fitting leads to significant improvement in the associated uncertainties with fitted parameters for Pt−Pt, and Pt−Ni/Fe paths, especially the coordination number. The global fitting was also able to estimate the low average oxygen coordination number in the 800 °C treated catalyst. The assumption for this operation was that bond distance and bond disorder were the same for Pt−O, Pt−Ni, or Pt−Pt in Pt alloys annealed at two different temperatures, 400 and 800 °C, which is greatly supported by the individual fittings (see Table S1). As shown in Table 2, some Pt is in oxide form. It is also clearly shown that the majority of the nearest neighbors around Pt are Pt regardless of the fitting model used. Although the PtNi model gives a slightly smaller R-factor than does the PtFe model, the difference is small so we cannot conclude that only Ni exists in the Pt coordination shell, but rather the fitting results strongly suggest coexistence of Ni and Fe in the Pt alloy because both models fit the data very well. Thus, the EXAFS data confirm the formation of PtNiFe alloy, and the coordination number of Ni in PtNi model or Fe in PtFe model is better interpreted as the total coordination number of Ni and Fe in the first coordination shell of Pt. Table 2 shows that the PtNi model results in a bigger total coordination number of Ni and Fe than does the PtFe model.

The global fitting results show that regardless of fitting model and within the uncertainties, there is a relatively more significant increase in the coordination number of Ni/Fe than that of Pt with increasing temperature. For example, based on the PtNi model, the Pt CN for PtNiFe/C annealed at 400 °C

Table 2. Structural Parameters Obtained from Global Fitting of Pt L3 Edge EXAFS Data for $Pt_{46}Ni_{22}Fe_{32}$/C Annealed at 400 and 800 °C Using the PtNi and PtFe Models

catalyst	scattering path	*N*, coordination number	*R*, bond length (Å)	Debye− Waller factor (10^{-3} Å^2)	*R*-factor
Pt L3 Edge (Fitting with PtNi Model)					
400 °C	Pt−O	0.4 ± 0.1	1.97 ± 0.03	5.8 ± 4.3	0.00120
	Pt−Ni	4.1 ± 0.2	2.64 ± 0.00	8.0 ± 0.4	
	Pt−Pt	5.3 ± 0.3	2.71 ± 0.00	5.6 ± 0.2	
800 °C	Pt−O	0.15 ± 0.07	1.97 ± 0.03	5.8 ± 4.3	
	Pt−Ni	5.4 ± 0.3	2.64 ± 0.00	8.0 ± 0.4	
	Pt−Pt	6.3 ± 0.3	2.71 ± 0.00	5.6 ± 0.2	
Pt L3 Edge (Fitting with PtFe Model)					
400 °C	Pt−O	1.1 ± 0.4	1.98 ± 0.06	21.6 ± 10.0	0.00214
	Pt−Fe	3.1 ± 0.2	2.65 ± 0.00	5.6 ± 0.5	
	Pt−Pt	5.0 ± 0.4	2.71 ± 0.00	5.2 ± 0.3	
800 °C	Pt−O	0.8 ± 0.3	1.98 ± 0.06	21.6 ± 10.0	
	Pt−Fe	4.0 ± 0.3	2.65 ± 0.00	5.6 ± 0.5	
	Pt−Pt	5.9 ± 0.4	2.71 ± 0.00	5.2 ± 0.3	

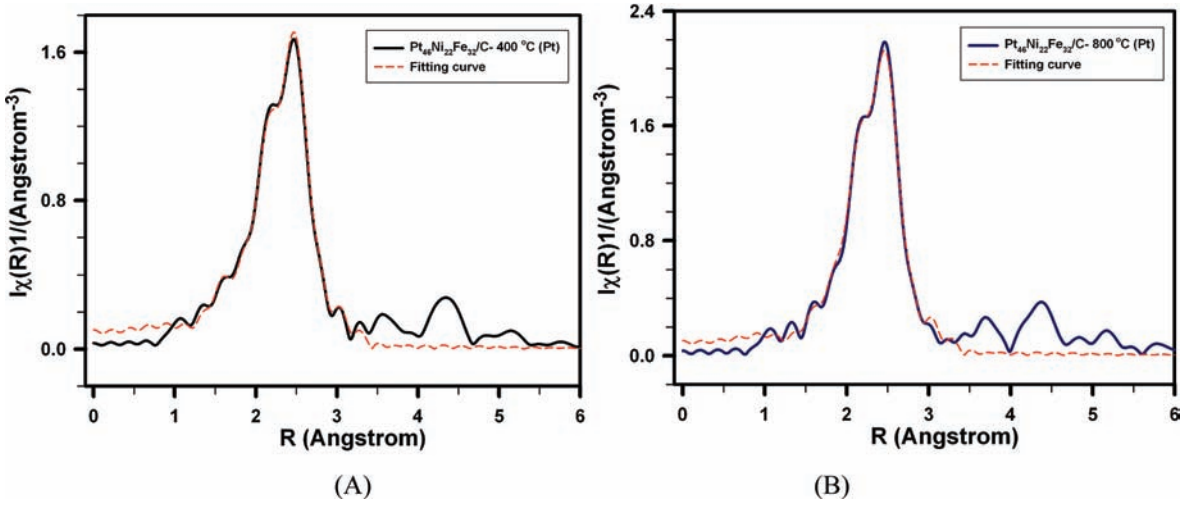

Figure 6. Original and fitted magnitude of Fourier transformed k^2-weighted Pt L3 edge EXAFS spectra of $Pt_{46}Ni_{22}Fe_{32}$ catalysts annealed at 400 °C (A) and 800 °C (B) from global fitting using Pt−Ni model.

(5.3) increases upon annealing the catalyst at 800 °C (6.3) (about 20% increase). Meanwhile, the Ni/Fe CN increases from 400 °C (4.1) to 800 °C (5.4) (about 32% increase). A similar difference is also observed from the PtFe model. Growth of particle size may cause an increase in the coordination number, and it should affect all neighbors similarly; thus a more significant increase in the coordination number of Ni/Fe than that of Pt indicates an increased degree of alloying between Pt and Ni/Fe.

For the case of oxygen, the obtained results are similar from the two models. As shown in Table 2, regardless of the model used, the fitted coordination number of O decreases when the catalyst was treated at higher temperature (800 °C). For example, the number decreases from 0.4 at 400 °C to 0.15 at 800 °C based on the PtNi model, and from 1.1 to 0.8 based on the PtFe model. The main difference in the results from the two models is the bigger uncertainties associated with the fitted coordination number from the PtFe model. Consequently, the results from the PtNi model show an obvious reduction in O coordination number, whereas the PtFe model suggests no significant change. Careful examination of other fitted parameters provides more insight. The fitted Debye−Waller factor (DWF) is also quite different from the two models. The number obtained using the PtFe model is somehow too high (21.6 × 10^{-3} Å^2) when compared to the much more reasonable value (5.8 × 10^{-3} Å^2) reported using the PtNi model. Therefore, for oxygen, we tend to trust the results obtained from the PtNi model, which clearly suggests a reduction in the Pt oxide when the catalyst is treated at higher temperature (800 °C).

There seems to be a discrepancy between the XRD and XAFS measurements for this trimetallic catalyst system as a function of thermal treatment temperature. XRD reports a small lattice shrinking estimated from the diffraction peaks, while EXAFS analysis shows no change in Pt−Pt bond distance. Note that EXAFS probes short-range order, and it is element specific and measures the coordination structure (including bond distance) around a specific element. Because O, Ni/Fe, and Pt have completely different scattering features, their bond distances to Pt are determined very accurately. Individual fittings of the Pt

Table 3. Structural Parameters Obtained from the Global Fitting of Ni K Edge EXAFS Data Using the NiNi and NiFe Models for $Pt_{46}Ni_{22}Fe_{32}$/C Annealed at 400 and 800 °C

catalyst	scattering path	*N*, coordination number	*R*, bond length (Å)	Debye− Waller factor (10^{-3} Å^2)	*R*-factor
Ni K Edge (Based on the NiNi Model)					
400 °C	Ni−O	1.3 ± 0.2	2.02 ± 0.03	1.6 ± 2.0	0.0217
	Ni−Ni	1.9 ± 0.8	2.64 ± 0.01	9.2 ± 4.1	
	Ni−Pt	5.4 ± 0.7	2.64 ± 0.01	7.5 ± 1.0	
800 °C	Ni−O	0.7 ± 0.2	2.02 ± 0.02	1.6 ± 2.0	
	Ni−Ni	2.5 ± 1.0	2.64 ± 0.01	9.2 ± 4.1	
	Ni−Pt	5.8 ± 0.8	2.64 ± 0.01	7.5 ± 1.0	
Ni K Edge (Based on the NiFe Model)					
400 °C	Ni−O	1.4 ± 0.2	2.02 ± 0.03	2.1 ± 2.1	0.0222
	Ni−Fe	1.2 ± 0.5	2.64 ± 0.01	5.3 ± 3.2	
	Ni−Pt	5.5 ± 0.7	2.64 ± 0.01	7.9 ± 1.1	
800 °C	Ni−O	0.8 ± 0.2	2.02 ± 0.02	2.1 ± 2.1	
	Ni−Fe	1.6 ± 0.6	2.64 ± 0.01	5.3 ± 3.2	
	Ni−Pt	5.9 ± 0.8	2.64 ± 0.01	7.9 ± 1.1	

EXAFS data for 400 and 800 °C treated samples showed an identical Pt−Pt bond distance even with different fitting models (Supporting Information, Table S1). In contrast, XRD examines long-range order, and the measured lattice constants describe the dimensions of a unit cell. Metals of same crystal structure and very similar lattice constant (e.g., Ni and Pt) tend to form alloy in a large composition range. Assuming that the Pt alloy possesses an identical crystal structure in the 400 and 800 °C treated samples, their unit cells would contain same number of atoms. As shown by EXAFS data, the 800 °C treated sample exhibits an increased alloying between Pt and Ni/Fe, suggesting that in its unit cell more smaller-sized atoms (Ni and Fe) are present than in that of the 400 °C treated sample, which effectively decreases the volume of the unit cell. The slight decrease in the lattice constant for the high temperature treated catalyst is consistent with an increased degree of alloying between Pt and Ni/Fe as supported by EXAFS data. In this regard, XRD and XAFS measurements are not contradictory but rather complementary.

Ni Coordination Structure. To effectively reduce uncertainties associated with fitted parameters, we also performed global fitting with the Ni K edge EXAFS data for the PtNiFe/C catalysts treated at 400 and 800 °C. Similar to the fitting process for the Pt EXAFS data, we also use two different fitting models. One uses O, Pt, and Ni as neighbors in the first coordination shell around Ni (NiNi model), and the other uses O, Pt, and Fe (NiFe model). Fitted parameters from the global fitting of the Ni K edge EXAFS data are presented in Table 3. The original and fitted magnitudes of Fourier transformed k^2-weighted Ni K edge EXAFS spectra (using the NiNi model) are shown in Figure 7.

A quick comparison of the fitting results from Pt L3 edge EXAFS data (Table 2) and that from the Ni K-edge data (Table 3) shows that the uncertainties associated with the fitted parameters from the Ni K edge EXAFS data are higher than those from the Pt data, which is consistent with the lower quality of the Ni data and its smaller range of chi data in the fitting, as shown in Supporting Information Figure S5, which includes chi values for all spectra. In addition, little conclusion can be drawn about the coordination of Ni or Fe around Ni. Despite these drawbacks, the Ni K edge EXAFS data provide very useful information about O and Pt coordination around Ni.

The global fitting results show that regardless of fitting model and within the uncertainties, the average coordination number of O is lower for the higher temperature treated catalyst. For example, based on the NiNi model, a certain decrease of the O coordination number is observed from 1.2 (±0.2) at 400 °C to 0.7 (±0.2) at 800 °C. A similar trend is also observed with the NiFe model. Thus, both models suggest that less Ni oxide is present in the high temperature treated sample, which is consistent with the XANES data.

The most important result from the Ni K edge EXAFS is the Pt coordination structure around Ni. As shown in Table 3, the fitting results of Pt are almost the same from the NiNi and NiFe models. This is a reflection of the fact that Pt is a much heavier element than the other neighbors, and with its unique scattering feature, the coordination of Pt around Ni can be reliably determined. The measured coordination numbers with uncertainties are 5.4 ± 0.7 for the 400 °C and 5.8 ± 0.8 for the 800 °C treated catalysts, respectively. One benefit of collecting both Pt L3 edge and Ni K edge EXAFS data on the same samples is that we have redundant measurement of coordination between Ni and Pt. The coordination number of Pt around Ni (denoted as CN (Ni−Pt), measured from Ni K edge) is determined by the number of Ni−Pt pairs divided by the total number of Ni. Similarly, the coordination number of Ni around Pt (denoted as CN (Pt−Ni), measured from Pt L3 edge) is determined by the number of Pt−Ni pairs divided by the total number of Pt. Because the number of Ni−Pt pairs is the same as the number of Pt−Ni pairs, thus CN (Ni−Pt)/CN (Pt−Ni) equals the total number of Pt divided by the total number of Ni, that is, 46/22 = 2.1. Therefore, the reliable value for CN (Pt−Ni) is 2.6 ± 0.3 for the catalyst treated at 400 °C or 2.8 ± 0.4 for catalyst treated at 800 °C, which suggests no significant change of CN with the treatment temperature or the alloying between Ni and Pt does not change with the temperature. Recall that we are only able to measure the total coordination number of Ni and Fe around Pt from Pt L3 edge EXAFS data because of their similarity (see Table 2), and now with the accurate determination of CN (Pt−Ni) from Ni K edge EXAFS data, we can study the alloying between Fe and Pt. Table 3 shows that there is an increase in the total coordination number of Ni and Fe of about 1 when the temperature is

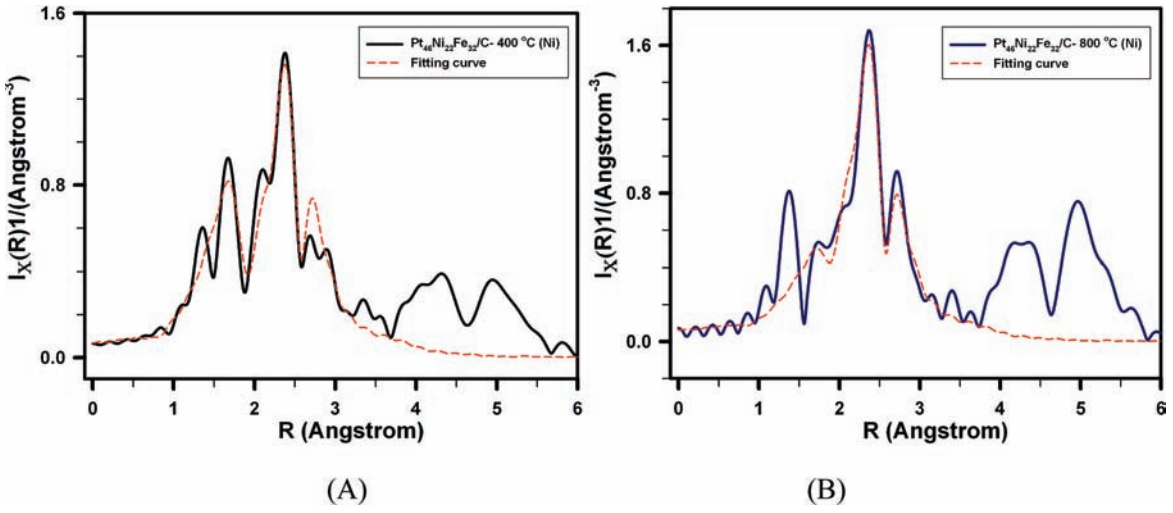

Figure 7. Original and fitted magnitudes of Fourier transformed k^2-weighted Ni K edge EXAFS spectra of $Pt_{46}Ni_{22}Fe_{32}$ catalysts annealed at 400 °C (A) and 800 °C (B) using global fitting based on the NiNi model.

increased from 400 to 800 °C regardless of the fitting model. This increase is most likely caused by better alloying of Fe with Pt because there is no significant change in the alloying between Ni and Pt. A quantitative assessment of the extent of alloying or atomic distribution in the nanoparticles was also attempted by analyzing the data (Supporting Information Figure S6 and Table S2) based on the methodology reported by Hwang et al. for determining the extent of alloying or atomic distribution in bimetallic nanoparticles.[43,44] While the analysis revealed some differences in relative Pt surface distribution between the catalysts treated at 400 and 800 °C, the large uncertainties of the current data prevented us from reaching a qualitative conclusion at this point in time.

Limited available Fe XAFS data have provided some additional insight into the catalyst structure, including the Fe K edge XANES spectra for the PtNiFe/C catalyst treated at 400 °C and the two Fe standards (Fe_3O_4 and Fe foil) (Supporting Information Figure S7). The spectrum of the catalyst is halfway between those of the foil and the oxide, suggesting a significant portion (~50%) of Fe is in oxide form, which may also explain why in the Pt coordination structure we did not observe plenty of Fe, as can be estimated by subtracting the CN(Pt−Ni) from the total Ni/Fe coordination number determined from Pt EXAFS. Fitting of the Fe K edge EXAFS data for the PtNiFe/C catalysts treated at 400 °C (Supporting Information Figure S8 and Table S3) confirms the formation of Fe oxide (about ~40% assuming the 6-coordinated Fe in the oxide) and the presence of Pt in the Fe coordination structure (although much higher uncertainties are associated with the fitted parameters when compared to the Pt and Ni results). The Fe XAFS data suggest that Fe oxide is more difficult to reduce at lower temperature than the Ni oxide (the oxygen coordination around Fe is almost twice that around Ni), and higher temperature promotes the reduction of Fe oxide, which may be the reason for better alloying between Pt and Fe at higher temperature.

Potentially, the fitting results can be further improved by performing global fitting of EXAFS data collected from all elements, which is especially true for simpler systems such as bimetallic systems. Ideally, one would hope to include all paths in a fitting model. For example, when fitting Pt EXAFS data, Pt−O, Pt−Ni, Pt−Fe, and Pt−Pt paths are included in the fitting. The dilemma is that Fe and Ni have very similar scattering features, and a tiny difference in atomic radius (about 0.005 Å). To reliably resolve this difference in R, a large range of chi(k) is required. With $\Delta r = 0.005$ Å, an estimate of Δk from $\Delta r^* \Delta k = \pi/2$ yields a value of 314 $Å^{-1}$, which is practically impossible. We did not perform global fitting using both Pt and the Ni spectra because in the "PtNi" model the Pt−Ni path represents both Pt−Ni and Pt−Fe scattering paths, whereas Ni−Pt represents only the Ni−Pt path. Therefore, we cannot assume common bond distance and bond disorder for Pt−Ni and Ni−Pt paths, which is the basis for performing global fitting using both Pt and Ni spectra. However, similar bond distance and different bond disorder are expected for Pt−Ni and Ni−Pt paths, as shown in Tables 2 and 3.

Regardless of the limitations, important conclusions are made from the EXAFS measurements about the change in the catalyst when exposed to high temperature treatment: (1) less oxides are formed for both Pt and Ni; (2) both Fe and Ni alloy with Pt; and (3) alloying between Ni and Pt does not change much, whereas alloying between Fe and Pt is improved.

3.3. Electrocatalysis−Structure Relationship. The electrocatalytic ORR activity for PtNiFe/C catalysts was examined. The actual loading of the nanoparticles on carbon support was determined by TGA method. The catalysts described in this Article had actual total metal loadings of 27% (400 °C) and 37% (800 °C) treated catalysts. The mass activity for ORR was normalized against the actual mass loading. In comparison with Pt/C, the PtNiFe/C catalysts treated at two different temperatures showed less-resolved features in the hydrogen adsorption/desorption and the platinum oxide oxidation/reduction regions (Figure 8A, inset).

The CV features in the potential region of 0−0.4 V (vs RHE) are characteristic of the hydrogen adsorption/desorption waves.[20] It is notable that in the hydrogen adsorption region (between 0−0.4 V), PtNiFe/C catalysts showed a very broad peak as compared to Pt/C. This difference likely reflects the different particle sizes, surfaces, and defects in these catalysts. The integration of charges under the hydrogen adsorption/desorption waves in the 0−0.4 region allowed us to measure

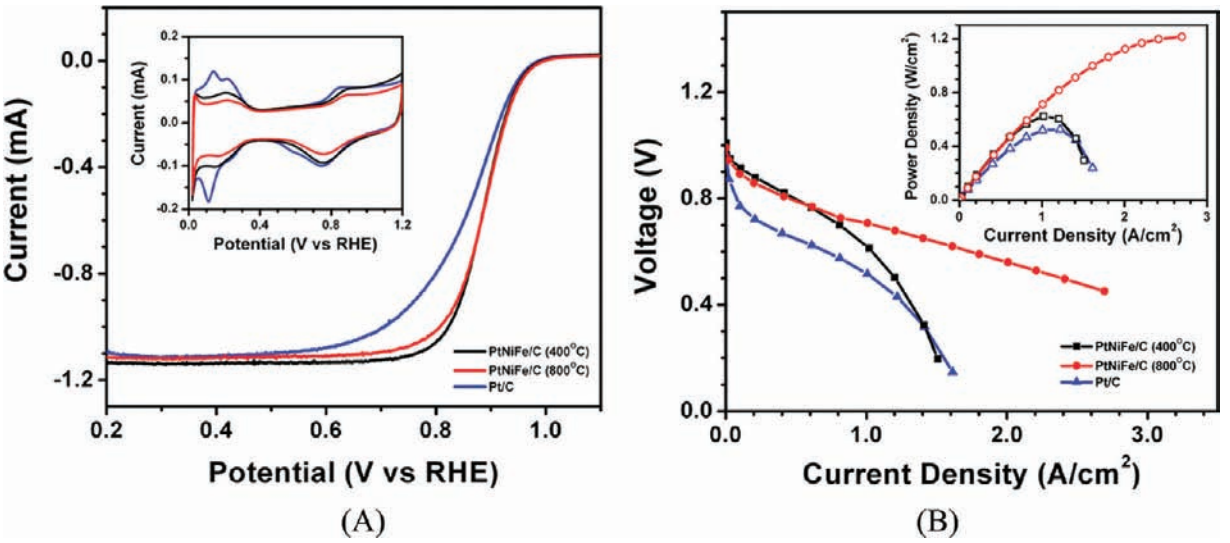

Figure 8. (A) RDE curves for $Pt_{46}Ni_{32}Fe_{32}/C$ catalysts treated at 400 and 800 °C. Electrode: Glassy carbon electrode inked with the catalysts. Electrolyte: 0.1 M $HClO_4$ saturated with O_2. Scan rate: 10 mV/s. Rotating speed: 1600 rpm. Inset: CV curves in 0.1 M $HClO_4$ (scan rate: 50 mV/s). (B) Polarization (●/■) and power density (○/□, see insert) curves of MEAs with $Pt_{46}Ni_{32}Fe_{32}/C$ catalysts (400 and 800 °C) or Pt/C (triangles) catalyst in the cathode in PEMFC at 75 °C. Pt loading in both anode and cathode was 0.4 mg_{Pt}/cm^2 for these MEAs.

the electrochemical active area (ECA) of the catalysts. In comparison with the ECA value of 90.1 m^2/g_{Pt} for Pt/C, the PtNiFe/C catalysts exhibited values of 53.4 and 26.5 m^2/g_{Pt} for the 400 and 800 °C treatments, respectively. The 800 °C treated catalyst showed a smaller value of ECA, which is consistent with the size increase of the catalyst particles. On the basis of TEM data for the $Pt_{46}Ni_{22}Fe_{32}/C$ catalysts treated at the two different temperatures, there is an increase in the average size of the particles (from 5.3 ± 0.4 nm at 400 °C to 7.8 ± 0.6 nm at 800 °C).

Figure 8A shows a representative set of RDE curves for the ORR activities at the PtNiFe/C catalysts in 0.1 M $HClO_4$ electrolyte. The measurement of the kinetics current at 0.9 V (vs RHE) showed values of 0.43 and 0.44 mA for the 400 and 800 °C treated PtNiFe catalysts, respectively. These values translate to a Pt-mass activity of 0.38 and 0.27 A/mg_{Pt} for the catalysts treated at 400 and 800 °C, respectively, which are higher than the Pt/C (0.22 A/mg_{Pt}), indicating that there is a higher electrocatalytic activity for the PtNiFe catalyst. Considering the differences in ECA, the specific activities of the PtNiFe/C catalysts treated at 400 and 800 °C are 0.71 and 1.02 mA/cm^2, respectively, which are 3−5 times Pt/C (0.24 mA/cm^2).

The trimetallic catalysts were evaluated in a PEM fuel cell to determine their fuel cell performances. Figure 8B shows a representative set of fuel cell performance data for MEAs loaded with PtNiFe/C and Pt/C catalysts under the loading of 0.4 mg_{Pt}/cm^2. The data between our catalysts and those using the commercial Pt/C catalyst were compared. As shown in the polarization curve obtained under 75 °C, the MEA with Pt/C catalyst exhibited a value of 0.52 V at 1.0 A/cm^2. This value is largely comparable to those reported under similar operational conditions using CCS method for the MEA fabrication,[45] thus validating the quality and effectiveness of our MEA preparation for the evaluation of the fuel cell performance in comparing PtNiFe/C (treated at 400 and 800 °C) and Pt/C catalysts.

It is evident that both the cell voltage and the power density (PD) for the fuel cell with the PtNiFe/C catalysts in the cathode are higher than those for the Pt/C catalyst under the same test conditions. In the activation region, it is noted that catalyst treated at 400 °C showed better performance than that treated at 800 °C. For example, at 0.85 V, the current density for Pt is 0.04 A/cm^2, while PtNiFe 400 °C showed 0.33 A/cm^2 and PtNiFe/C 800 °C showed 0.22 A/cm^2. Both PtNiFe catalysts showed 5−8 times higher current density than the Pt/C catalysts. This result is interesting considering the fact that in the RDE result the mass activity of the PtNiFe/C catalysts only showed less than 2-fold improvement than that for the Pt/C catalyst. In the ohmic and transport region, the PtNiFe/C catalyst treated at 800 °C showed a higher peak power density (1.21 W/cm^2) than that for the PtNiFe/C catalyst treated at 400 °C (0.62 W/cm^2). Peak power density for Pt/C catalyst was found to be 0.52 W/cm^2. The fuel cell with higher temperature treated catalyst showed a 130% increase in peak power density in comparison with that of Pt/C. These results demonstrate excellent performance of the PtNiFe/C catalysts in PEM fuel cell in comparison to the Pt/C catalyst. The finding is also consistent with the electrocatalytic activity trend revealed by the RDE data.

In the kinetic or activation-controlled region, the values of current density at 0.9 V in the fuel-cell (FC) data were used to calculate the mass activities of the catalysts, which were then compared to the mass activities determined by RDE. In Figure 9A, the mass activities obtained from the kinetic region at 0.9 V from IR-free fuel-cell $I-E_{cell}$ curves and the mass activities obtained from RDE curves at 0.9 V in 0.1 M $HClO_4$ electrolyte are compared for the PtNiFe/C catalysts treated at low and high treatment temperatures. In general, the mass activities obtained from RDE and the fuel-cell polarization data showed one trend (i.e., MA decreases with increasing temperature), whereas the specific activities obtained from RDE and the fuel-cell polarization data showed another trend (i.e., SA increases with increasing temperature). In Figure 9B, the peak power densities of the catalysts are compared to Pt catalyst. On the basis of the peak power density values obtained from the $I-P$ curves, the PtNiFe/C showed an enhanced electrocatalytic performance in the PEM fuel among these catalysts. It is important to note that the trend observed from comparing the mass activities between

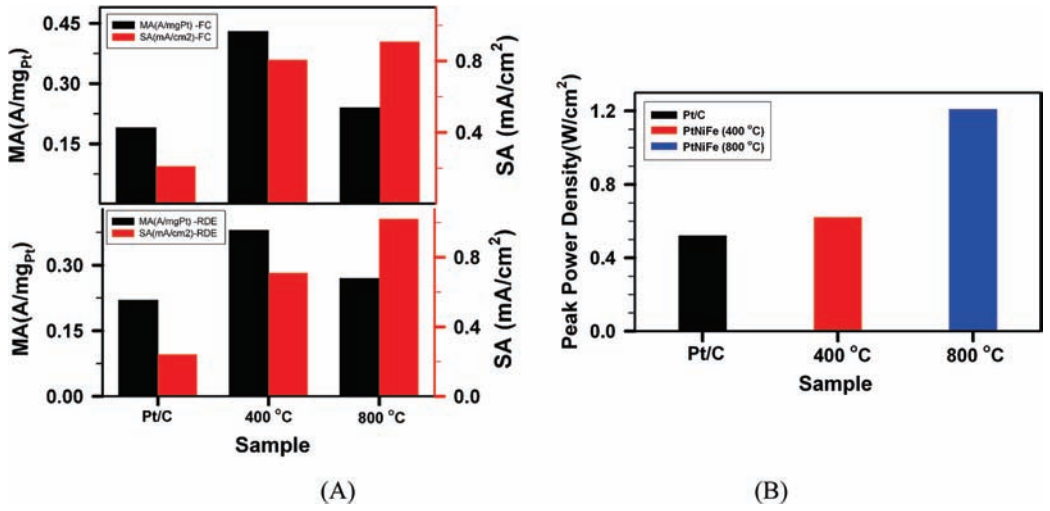

Figure 9. (A) Comparison of the mass activities obtained from the kinetic region at 0.9 V from IR-free fuel-cell (FC) $I-E_{cell}$ curves and the mass activities obtained from RDE curves at 0.9 V in 0.1 M $HClO_4$ electrolyte for the PtNiFe/C catalysts treated at 400 and 800 °C. (B) Comparison of the electrocatalytic performance data of the catalysts with Pt catalyst in terms of the peak power density values from the $I-P$ curves.

Table 4. Summary of the Electrocatalytic Activity Data from RDE and FC Measurements and the Structural Parameters Determined from XRD and XAFS Data and the Relative Surface Composition from the XPS Data[a]

	RDE		FC		XPS	XRD	XAFS
T (°C)	MA at 0.9 V (A/mg_{Pt})	SA at 0.9 V (mA/cm^2)	MA at 0.9 V (A/mg_{Pt})	PD (W/cm^2)	relative surface concentration	fcc-type lattice constant	atomic-scale metal oxides and alloy structure
400	0.38	0.71	0.43	0.62	46% Pt and 54% (Ni + Fe)	0.3798 nm	more oxides, less alloyed structure
800	0.27	1.02	0.25	1.21	43% Pt and 57% (Ni + Fe)	0.3780 nm	less oxides, more alloyed structure

[a] (a1) PtNi model; (a2) NiNi model; (b1) PtFe model; and (b2) NiFe model.

FC and RDE data in the kinetic region and the trend from the peak power densities in the ohmic and mass transport regions are not always consistent, reflecting the complexity in evaluating the electrocatalytic and fuel-cell performance of the catalysts. The 800 °C treated catalyst showed a lower mass activity than that for the 400 °C treated catalyst based on the kinetic current data from both RDE and FC $I-V$ curves. However, the 800 °C treated catalyst showed a higher performance than the 400 °C treated catalyst based on the $I-V$ data in the ohmic and transport regions for the fuel cell. This complexity has in fact been observed for the fuel-cell performance of other alloy catalysts treated differently.[46,47]

To develop the correlation between the electrocatalytic activities and the atomic scale structures determined from the XAFS measurements, Table 4 summarizes the electrocatalytic activity data from RDE and FC measurements and the structural parameters determined from the XRD and EXAFS data and the relative surface composition from the XPS data.

The mass activities from both RDE and FC-kinetic revealed a consistent trend; that is, the catalyst treated at 400 °C has a higher activity than the catalyst treated at 800 °C. The XRD-derived structures in terms of lattice reduction have provided a qualitative assessment for the electrocatalytic enhancement,[16] suggesting a trend of lattice strain in the 800 °C catalyst with a smaller lattice constant than the 400 °C treated catalyst. Pt—Pt bond distance was measured accurately by EXAFS, and no difference was observed (from individual fitting). Qualitatively, the Pt sites on the surface are relatively richer for the 400 °C treated catalyst than for the 800 °C treated catalyst, although they are less active for the former. Therefore, the lower-temperature treated catalyst is more active on a mass basis (i.e., the number of active sizes dominates). On the other hand, the specific activity data from RDE revealed an opposite trend; that is, the catalyst treated at the higher temperature showed a higher activity than the catalyst treated at the lower temperature. The higher specific activity for the higher temperature treated catalyst reflects the likelihood of a better Pt alloying with Fe or Ni. Considering that the specific activity is associated with the particle size and the surface Pt concentration, the difference in the surface metal oxides and alloying structures between the catalyst treated at 800 °C with a larger particle size (7.8 nm) and the catalyst treated at 400 °C with a smaller particle size (5.3 nm), as revealed by XAFS analysis, has demonstrated the significant role played by both particle size and surface atomic structure of the catalyst. Because the Pt—Pt distance does not seem to change, the electronic structure around Pt may be changed as a result of the better alloying of the surface Pt atoms with Ni or Fe, as evidenced by the change in the coordination numbers. Clearly, in addition to the particle size change, a combination of the increased alloy degree, reduced amount of metal oxides, and the enrichment of base metal components in the alloy surface for the higher temperature treated catalyst is responsible for the

increased specific activity. Part of our ongoing work involves examining how such atomic scale structural correlation impacts the catalyst stability and applies to other bimetallic and trimetallic alloy catalysts.[14,16]

4. CONCLUSION

The findings have provided new insights for assessing the atomic coordination structural correlation of the electrocatalytic activity of nanoengineered trimetallic catalysts treated under different temperatures for oxygen reduction reaction. In addition to electrochemical characterization, a detailed XAFS analysis of the atomic scale coordination structures revealed an increase in Pt−Ni(Fe) coordination number with improved alloying structure for the catalyst treated at elevated temperatures. The XPS data have revealed a reduced surface concentration of Pt for the catalyst for the high temperature treated catalyst. Taken together, the higher mass activity for the lower temperature treated catalyst is due to Pt surface enrichment on the surface sites, whereas the higher specific activity for the higher temperature treated catalyst reflects an enhanced Pt-alloying surface sites. The atomic scale structural and composition analyses have thus provided useful information for a comprehensive understanding of the lower mass activity and higher specific activity for the trimetallic catalyst treated at the elevated temperature. This understanding has also provided the basis for the atomic scale understanding of the enhanced electrocatalytic performance of this trimetallic catalyst in fuel cells.

■ ASSOCIATED CONTENT

Supporting Information. Additional information from TEM, XRD, and EXAFS data and analysis. This material is available free of charge via the Internet at http://pubs.acs.org.

■ AUTHOR INFORMATION

Corresponding Author
cjzhong@binghamton.edu; yzc2@psu.edu

■ ACKNOWLEDGMENT

This work was supported by the National Science Foundation (CBET-0709113, CHE 0848701). MRCAT operations are supported by the Department of Energy and the MRCAT member institutions. The XAFS work at the 9-BM Beamlines is supported in part by the Office of Basic Energy Sciences of the U.S. Department of Energy and by the National Science Foundation Division of Materials Research. Use of the Advanced Photon Source is supported by the Office of Basic Energy Sciences of the U.S. Department of Energy under Contract No. W-31-109-Eng-38. The XPS was performed using EMSL, a national scientific user facility sponsored by the Department of Energy's Office of Biological and Environmental Research located at Pacific Northwest National Laboratory. We also thank Dr. H. R. Naslund for assistance in DCP-AES analysis, and Dr. I.-T. Bae for assistance in HRTEM analysis.

■ REFERENCES

(1) Gasteiger, H. A.; Kocha, S. S.; Sompalli, B.; Wagner, F. T. *Appl. Catal., B* **2005**, *56*, 9–35.

(2) Zhong, C. J.; Luo, J.; Njoki, P. N.; Mott, D.; Wanjala, B.; Loukrakpam, R.; Lim, S.; Wang, L.; Fang, B.; Xu, Z. C. *Energy Environ. Sci.* **2008**, *1*, 454–466.

(3) Stamenkovic, V. R.; Mun, B. S.; Arenz, M.; Mayrhofer, K. J. J.; Lucas, C. A.; Wang, G. F.; Ross, P. N.; Markovic, N. M. *Nat. Mater.* **2007**, *6*, 241–247.

(4) Stamenkovic, V.; Schmidt, T. J.; Ross, P. N.; Markovic, N. M. *J. Electroanal. Chem.* **2003**, *554*, 191–199.

(5) Paulus, U. A.; Wokaun, A.; Scherer, G. G.; Schmidt, T. J.; Stamenkovic, V.; Radmilovic, V.; Markovic, N. M.; Ross, P. N. *J. Phys. Chem. B* **2002**, *106*, 4181–4191.

(6) Greeley, J.; Stephens, I. E. L.; Bondarenko, A. S.; Johansson, T. P.; Hansen, H. A.; Jaramillo, T. F.; Rossmeisl, J.; Chorkendorff, I.; Norskov, J. K. *Nat. Chem.* **2009**, *1*, 552–556.

(7) Stamenkovic, V. R.; Fowler, B.; Mun, B. S.; Wang, G. F.; Ross, P. N.; Lucas, C. A.; Markovic, N. M. *Science* **2007**, *315*, 493–497.

(8) Stamenkovic, V.; Schmidt, T. J.; Ross, P. N.; Markovic, N. M. *J. Phys. Chem. B* **2002**, *106*, 11970–11979.

(9) Mukerjee, S.; Srinivasan, S.; Soriaga, M. P.; McBreen, J. *J. Electrochem. Soc.* **1995**, *142*, 1409–1422.

(10) Toda, T.; Igarashi, H.; Uchida, H.; Watanabe, M. *J. Electrochem. Soc.* **1999**, *146*, 3750–3756.

(11) Toda, T.; Igarashi, H.; Watanabe, M. *J. Electroanal. Chem.* **1999**, *460*, 258–262.

(12) Wanjala, B. N.; Luo, J.; Loukrakpam, R.; Fang, B.; Mott, D.; Njoki, P. N.; Engelhard, M.; Naslund, H. R.; Wu, J. K.; Wang, L. C.; Malis, O.; Zhong, C. J. *Chem. Mater.* **2010**, *22*, 4282–4294.

(13) Wanjala, B. N.; Luo, J.; Fang, B.; Mott, D.; Zhong, C. J. *J. Mater. Chem.* **2011**, *21*, 4012–4020.

(14) Loukrakpam, R.; Luo, J.; He, T.; Chen, Y.; Xu, Z.; Njoki, P. N.; Wanjala, B. N.; Fang, B.; Mott, D.; Yin, J.; Klar, J.; Powell, B.; Zhong, C. J. *J. Phys. Chem. C* **2011**, *115*, 1682–1694.

(15) Loukrakpam, R.; Chang, P.; Luo, J.; Fang, B.; Mott, D.; Bae, I. T.; Naslund, H. R.; Engelhardd, M. H.; Zhong, C. J. *Chem. Commun.* **2010**, *46*, 7184–7186.

(16) Wanjala, B. N.; Loukrakpam, R.; Luo, J.; Njoki, P. N.; Mott, D.; Zhong, C. J.; Shao, M. H.; Protsailo, L.; Kawamura, T. *J. Phys. Chem. C* **2010**, *114*, 17580–17590.

(17) Fang, B.; Luo, J.; Chen, Y.; Wanjala, B. N.; Loukrakpam, R.; Hong, J.; Yin, J.; Hu, X.; Hu, P.; Zhong, C. J. *ChemCatChem* **2011**, *3*, 583–593.

(18) Fang, B.; Wanjala, B. N.; Hu, X. A.; Last, J.; Loukrakpam, R.; Yin, J.; Luo, J.; Zhong, C. J. *J. Power Sources* **2011**, *196*, 659–665.

(19) Fang, B.; Luo, J.; Njoki, P. N.; Loukrakpam, R.; Wanjala, B.; Hong, J.; Yin, J.; Hu, X.; Last, J.; Zhong, C. J. *Electrochim. Acta* **2010**, *55*, 8230–8236.

(20) Fang, B.; Luo, J.; Njoki, P. N.; Loukrakpam, R.; Mott, D.; Wanjala, B.; Hu, X.; Zhong, C. J. *Electrochem. Commun.* **2009**, *11*, 1139–1141.

(21) Luo, J.; Han, L.; Kariuki, N. N.; Wang, L. Y.; Mott, D.; Zhong, C. J.; He, T. *Chem. Mater.* **2005**, *17*, 5282–5290.

(22) Luo, J.; Kariuki, N.; Han, L.; Wang, L.; Zhong, C. J.; He, T. *Electrochim. Acta* **2006**, *51*, 4821–4827.

(23) He, T.; Kreidler, E.; Xiong, L.; Luo, J.; Zhong, C. J. *J. Electrochem. Soc.* **2006**, *153*, A1637–A1643.

(24) Luo, J.; Wang, L. Y.; Mott, D.; Njoki, P. N.; Kariuki, N.; Zhong, C. J.; He, T. *J. Mater. Chem.* **2006**, *16*, 1665–1673.

(25) Wei, Z. D.; Feng, Y. C.; Li, L.; Liao, M. J.; Fu, Y.; Sun, C. X.; Shao, Z. G.; Shen, P. K. *J. Power Sources* **2008**, *180*, 84–91.

(26) Yu, P.; Pemberton, M.; Plasse, P. *J. Power Sources* **2005**, *144*, 11–20.

(27) Tamizhmani, G.; Capuano, G. A. *J. Electrochem. Soc.* **1994**, *141*, 968–975.

(28) Mani, P.; Srivastava, R.; Strasser, P. *J. Power Sources* **2011**, *196*, 666–673.

(29) Seo, A.; Lee, J.; Han, K.; Kim, H. *Electrochim. Acta* **2006**, *52*, 1603–1611.

(30) Shim, J.; Yoo, D. Y.; Lee, J. S. *Electrochim. Acta* **2000**, *45*, 1943–1951.

(31) Chen, Y. S.; Fulton, J. L.; Partenheimer, W. *J. Solution Chem.* **2005**, *34*, 993–1007.

(32) Ravel, B.; Newville, M. *J. Synchrotron Radiat.* **2005**, *12*, 537–541.
(33) Newville, M. *J. Synchrotron Radiat.* **2001**, *8*, 96–100.
(34) Rehr, J. J.; Albers, R. C. *Rev. Mod. Phys.* **2000**, *72*, 621–654.
(35) Arico, A. S.; Shukla, A. K.; Kim, H.; Park, S.; Min, M.; Antonucci, V. *Appl. Surf. Sci.* **2001**, *172*, 33–40.
(36) Shukla, A. K.; Neergat, M.; Bera, P.; Jayaram, V.; Hegde, M. S. *J. Electroanal. Chem.* **2001**, *504*, 111–119.
(37) Shukla, A. K.; Raman, R. K.; Choudhury, N. A.; Priolkar, K. R.; Sarode, P. R.; Emura, S.; Kumashiro, R. *J. Electroanal. Chem.* **2004**, *563*, 181–190.
(38) Yang, D. Q.; Sacher, E. *J. Phys. Chem. C* **2009**, *113*, 6418–6425.
(39) Nurmi, J. T.; Tratnyek, P. G.; Sarathy, V.; Baer, D. R.; Amonette, J. E.; Pecher, K.; Wang, C. M.; Linehan, J. C.; Matson, D. W.; Penn, R. L.; Driessen, M. D. *Environ. Sci. Technol.* **2005**, *39*, 1221–1230.
(40) Mathieu, H. J.; Landolt, D. *Corros. Sci.* **1986**, *26*, 547–559.
(41) Millis, P.; Sullivan, J. L. *J. Phys. D* **1983**, *16*, 723.
(42) Allen, G. C.; Curtis, M. T.; Hooper, A. J.; Tucker, P. M. *J. Chem. Soc., Dalton Trans.* **1974**, 1525.
(43) Lai, F.-J.; Sarma, L. S.; Chou, H.-L.; Liu, D.-G.; Hsieh, C.-A.; Lee, J.-F.; Hwang, B.-J. *J. Phys. Chem. C* **2009**, *113*, 12674–12681.
(44) Hwang, B.-J.; Sarma, L. S.; Chen, J.-M.; Chen, C. H.; Shih, S.-C.; Wang, G.-R.; Liu, D.-G.; Lee, J.-F.; Tang, M.-T. *J. Am. Chem. Soc.* **2005**, *127*, 11140–11145.
(45) Prasanna, M.; Cho, E. A.; Lim, T. H.; Oh, I. H. *Electrochim. Acta* **2008**, *53*, 5434–5441.
(46) Bianchini, C.; Shen, P. K. *Chem. Rev.* **2009**, *109*, 4183–4206.
(47) Wang, C. Y. *Chem. Rev.* **2004**, *104*, 4727–4765.